

# Analysis and Design of Synchronous Machines with Reluctance Rotor and PM Stator Combined Excitation

Oluwaseun A. Badewa, and Dan M. Ionel

SPARK Laboratory, Stanley and Karen Pigman College of Engineering, University of Kentucky, Lexington, KY, USA  
o.badewa@uky.edu, dan.ionel@ieee.org

**Abstract**—This paper studies motors that are part of a general class of synchronous machines with stator-only excitation including those that may be referred to in recent literature as of the flux switching, variable flux reluctance, or hybrid excitation type. In the studied example machine, the active stator has circumferentially magnetized spoke-type PMs and concentrated toroidal coils for improved slot fill and shortened end turns. A systematic analysis of the mmf produced by the toroidal coils in the stator and open-circuit airgap flux is developed to define feasible polarities of this synchronous motor and to establish that the dominant pole pair number is a consequence of the number of rotor protrusions. Several methods are employed for determining the d- and q-axes inductances and it is shown that the machine displays a non-salient behavior despite its castellated rotor. Analytical calculations and the 2-D FEA results are validated using experimental results obtained from the motor prototype.

**Index Terms**—Parameter identification, synchronous motor, flux intensifying machine, active-stator, permanent magnet (PM) machine, d- and q-axis inductances, castellated rotor, spoke-type PM, finite element analysis.

## I. INTRODUCTION

In recent years, there has been a surge of interest in the development of specialty high-power dense motors with permanent magnets (PMs) for applications where space and weight constraints are critical [1], [2]. In electric vehicles (EV), for example, approximately 80 - 90% of currently deployed EV traction motors employ rare-earth permanent magnets (PM) owing to their high coercivity, thermal characteristics, and high energy product (BH) max [3], [4].

The growing concerns about the availability and geopolitical risks associated with rare-earth permanent magnets (PMs) have spurred increased research and innovation in alternative materials for electric motor applications. Non-rare earth PMs and innovative PM materials such as iron nitride PMs are being explored for long-term sustainable development of PM motors [5]–[8]. One consequence of employing non-rare earth PMs is a reduction in the energy product relative to rare-earth PMs, potentially reducing overall power density.

Specialty topologies such as the “spoke” type interior permanent magnet (IPM) configuration can increase magnetic loading to enhance specific power capability and magnetic loading with non-rare earth PMs. A specialty spoke-type synchronous machine with radially oriented and tangentially magnetized PMs has been proposed prior to allow for increased

specific power with non-rare earth PMs. This topology can be utilized in conjunction with, for example, flux barriers in the q-axis [9], special stator tooth profiles [10], and high-polarity fraction slot pole combinations [11] for further performance improvement.

Demagnetization risks associated with PM overheating and the effect of the armature field can be addressed by implementation of effective stator-only cooling with PMs placed in a flux-focusing “spoke” arrangement in the stator alongside the armature windings [12], [13]. Also, the positioning of all active elements in the stator allows for a simple reluctance-type rotor capable of high-speed operation.

The proposed machine is of the synchronous type with an AC multi-phase winding in the stator fed with sine wave-regulated currents. The excitation is provided by the combination of stator PMs and rotor reluctance as described in subsequent sections. This machine has a special winding with toroidal compact concentrated coils effectively corresponding to a fully-pitched distributed winding with the advantages of reduced losses from shortened end turns and overall compact design for high power density [14].

In this paper, investigations into the topology, operating principle, effects of non-linearity, and parameterization of a synchronous motor are carried out using theoretical formulations, harmonic analyses, FEA, and results from experimental tests [15].

## II. MOTOR TOPOLOGY, DESIGN, AND OPERATING PRINCIPLE

Operating principles for machines with hybrid excitation can be derived through analysis of the topology and application of phenomenological analysis. The example studied machine has an active outer stator that contains circumferentially magnetized PMs, concentrated toroidal windings for improved copper slot fill and reduced losses due to shortened end turns, and a castellated consequent pole rotor as shown in Fig. 1a. It can also be modeled in an outer rotor configuration which enables flux intensification through an increased flux concentration ratio by using longer PMs in the inner stator. The absence of active elements in the castellated rotor allows for high-speed operations and application of advanced cooling [16].

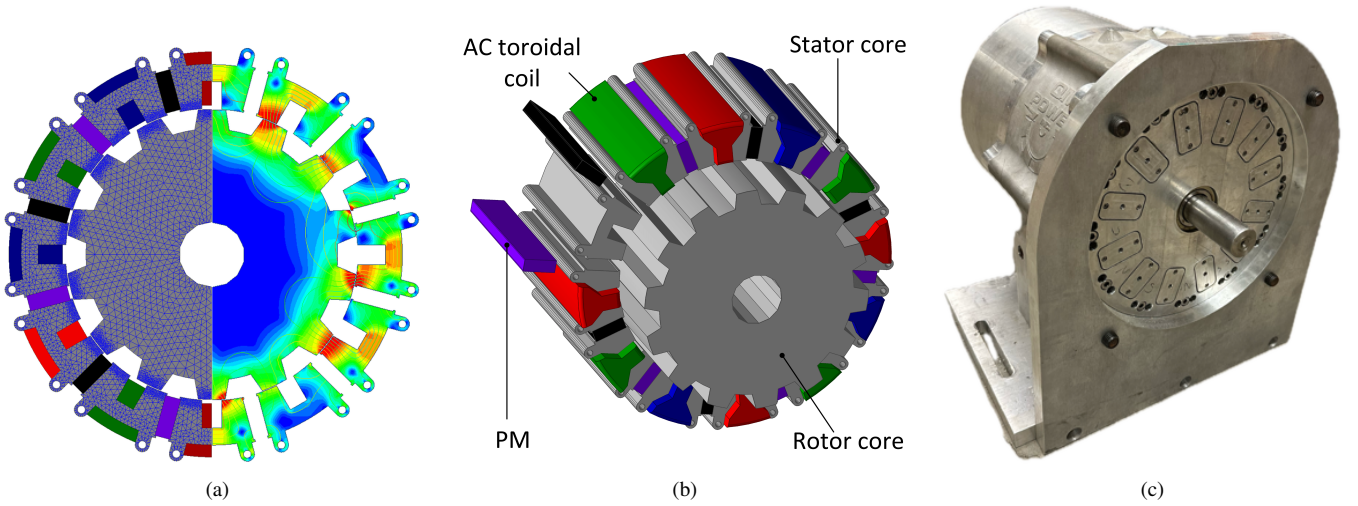


Fig. 1. (a) Finite element analysis (FEA) model of studied synchronous motor showing mesh, flux lines, and densities, (b) 3D model of proposed PM motor with active outer stator and castellated rotor, and (c) the constructed prototype of the synchronous motor.

Assuming infinite permeability in the rotor in the direction of the green arrow such that the concept of a half airgap is associated with the stator and the other half associated with the rotor as shown in Fig. 2, a study of the stator and the mmf field produced by the armature windings provides insight into the polarity and working slot-pole combinations of this synchronous machine. The stator permeance,  $\Lambda_s$ , considering the slots, PMs, and teeth positions starting from the reference axis as shown in Fig. 2 can then be quantitatively summarized in:

$$\Lambda_s(\theta) = \begin{cases} \Lambda_{k_{\min}}, & \theta \in (\theta - \frac{\beta_k}{2}, \theta + \frac{\beta_k}{2}) \\ \Lambda_{PM_{\min}}, & \theta \in (\theta - \frac{\beta_{PM}}{2}, \theta + \frac{\beta_{PM}}{2}) \\ \Lambda_{st_{\max}}, & \theta \in (\theta - \frac{\beta_{st}}{2}, \theta + \frac{\beta_{st}}{2}), \end{cases} \quad (1)$$

where  $\theta$  is the angular displacement along the stator periphery,  $\beta_k$ ,  $\beta_{PM}$ , and  $\beta_{st}$  are the angular coordinates of stator slots, PMs, and teeth respectively. All angles are in mechanical radians. Minimum values of permeance denoted by  $\Lambda_{k_{\min}}$  and  $\Lambda_{PM_{\min}}$  correspond to the maximum airgap under the slots and PMs respectively, while the maximum permeance,  $\Lambda_{st_{\max}}$ , corresponds to the minimum airgap under the stator teeth.

Considering  $N_{ck}$  conductors in a slot  $k$  located at an angular coordinate  $\theta_k$  measured in mechanical radians, the linear current density produced at the airgap can be expressed as:

$$\begin{cases} J_{Lk}(\theta, t) = \frac{2N_{ck}i_k(t)}{\beta_k D}, & \theta \in (\theta - \frac{\beta_k}{2}, \theta + \frac{\beta_k}{2}) \\ J_{Lk}(\theta, t) = 0, & \theta \notin (\theta - \frac{\beta_k}{2}, \theta + \frac{\beta_k}{2}), \end{cases} \quad (2)$$

where  $\beta_k$  is the angular slot opening,  $i_k(t)$  is the current flowing through the conductors and  $D$  is the stator diameter at the airgap surface. all angles are measured in mechanical radians [17].

If all slots are considered to have the same slot opening, the air gap mmf for phase A is given by the summation of all

slot contributions such that:

$$F_a(\theta, t) = \frac{2}{\pi} T_{ph} i_a(t) \sum_{v=1}^{\infty} \frac{k_{ov} k_{wv}}{v} * \sin v(\theta - \theta_{av}), \quad (3)$$

with:

$$k_{kov} = \frac{2}{v\beta_k} \sin \frac{v\beta_k}{2}, \quad (4)$$

$$k_{wv} = \frac{1}{2T_{ph}} \sqrt{\left( \sum_{k=1}^{Z_l} N_{sk} \sin v\theta_k \right)^2 + \left( \sum_{k=1}^{Z_l} N_{sk} \cos v\theta_k \right)^2}, \quad (5)$$

$$\theta_{av} = \frac{1}{v} \arctan \left[ \frac{\sum_{k=1}^{Z_l} N_{sk} \sin v\theta_k}{\sum_{k=1}^{Z_l} N_{sk} \cos v\theta_k} \right], \quad (6)$$

where  $v$  is the harmonic order,  $N_{sk}$  is the total number of series conductors in slot  $k$ ,  $T_{ph}$  is the number of series turns per phase,  $Z_l$  is the number of stator slots,  $k_{wv}$  is the harmonic winding factor, and  $k_{ov}$  is the overall slot opening harmonic factor which reaches the unity value for infinitely thin slots [17].

Using the forward and backward wave theory, for an  $m$ -phase symmetrical system with  $p$  pole pairs, the total air gap mmf produced can be obtained as:

$$F(\theta, t) = \frac{m}{\pi} T_{ph} I \sqrt{2} \sum_{v=1}^{\infty} \frac{k_{ov} k_{wv}}{v} * \{k_{fv} \cos [\omega t - v(\theta - \theta_{av})] + k_{bv} \cos [\omega t + v(\theta - \theta_{av})]\}, \quad (7)$$

where  $k_{fv, bv}$  are the forward and backward coefficients:

$$k_{fv, bv} = \frac{1}{m} \left[ 1 + (m-1) \cos(v \mp p) \frac{2\pi}{mp} \right]. \quad (8)$$

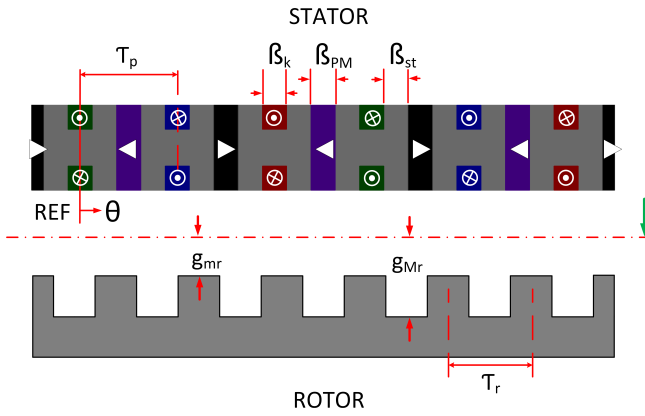


Fig. 2. Linear half-airgap model of studied motor showing a reference axis, airgap descriptions, stator, and rotor pole pitches, as well as angular coordinates of stator slots, teeth, and PMs. The horizontal dotted line is positioned at the center of the airgap.

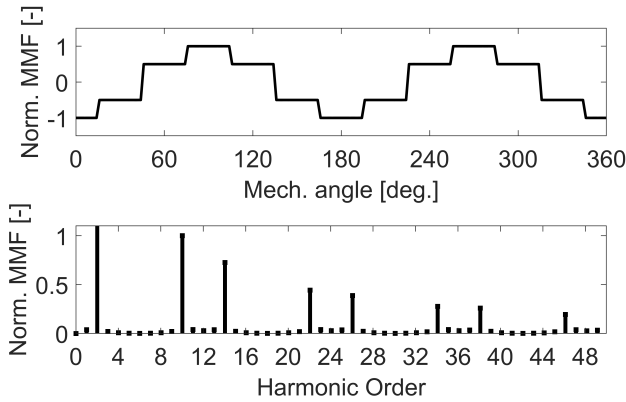


Fig. 3. The plot of overall mmf  $F_{a,b,c}(\theta, t)$  and its harmonic decomposition showing 10 and 14 as feasible pole pair numbers for this example 24-slot 3-ph synchronous machine with AC toroidal windings.

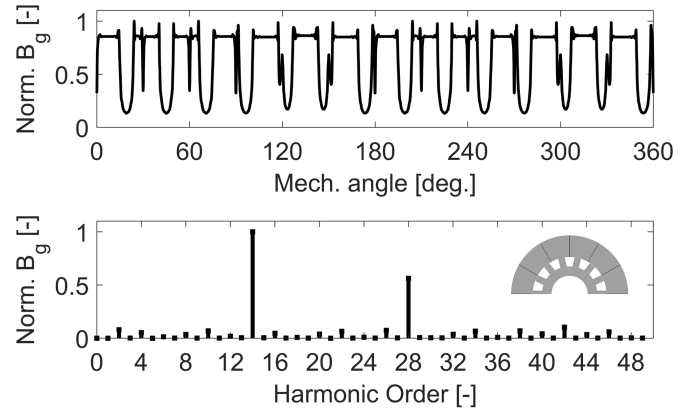
Using (3)-(8), the overall mmf produced by the 3-ph AC toroidal coils in this machine can be obtained as shown in Fig. 3 and its harmonic analysis shows 10 and 14 are feasible pole pair numbers for this 24-slot example machine. Also, the toroidal 3-phase winding is equivalent to a full-pitched winding with a unity winding factor.

The specific relationship between the number of rotor poles, stator slots, and armature poles is established as:

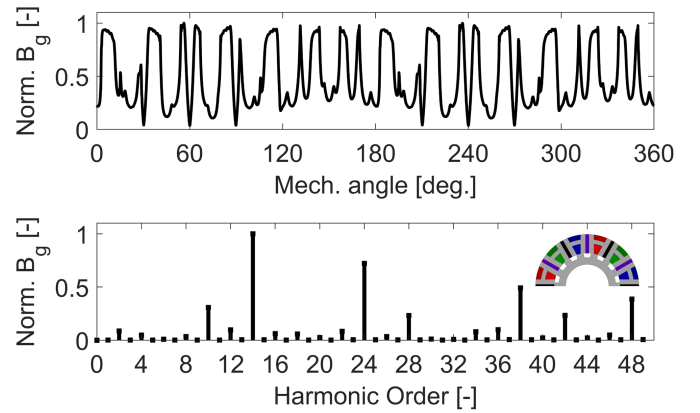
$$n \frac{Z_l}{m} = \pm 2N_{pr} \mp \frac{Z_l}{2}, \quad (9)$$

where  $n$  is an integer not divisible by 3, preferably 1 or 2, and  $N_{pr}$  is the number of rotor protrusions which is typically 5 or 7 for this 3-phase example machine [13].

Considering the modulus of the airgap flux density in a slotless stator with only PMs and a castellated rotor as shown in Fig. 4a, where the PMs are modeled very thin to separate their effect, i.e., slot opening of PMs on the open circuit airgap field and its harmonics, it can be observed that for



(a)



(b)

Fig. 4. Modulus of the airgap flux density calculated based on the radial and tangential components for the computational model with (a) very thin magnets and castellated rotor showing 14 as the dominant/principle pole pair number despite the 6-pole pair PM mmf, and (b) PMs, toroidal AC coils, stator, and castellated rotor illustrating that the largest harmonic component is the 14th.

this example machine despite the 6-pole pair PM mmf, the dominant pole pair number is 14 due to the rotor. A further study of the modulus of airgap flux density and its harmonic considering stator, 3-phase AC windings, PMs, and rotor in an energized state as shown in Fig. 4b establishes 14 as the principal number of pole pairs for this example synchronous motor consequent of the number of rotor protrusions,  $N_{pr}$ . The operational principle of this machine is based on parallel path magnetic technology and considerations for design and manufacturing are discussed in more detail in [14], [16].

### III. D-Q ANALYSIS, NON-LINEARITY, NON-SALIENCEY, AND EXPERIMENTAL RESULTS

The direct and quadrature axis inductances have a significant impact on the torque-producing capability and flux control of permanent magnet synchronous machines [18], [19]. These inductances also affect the efficiency and power factor of the machine and are useful for creating analytical models of electrical machines. There are different methods to calculate

Table I  
SPECIFICATIONS AND MAIN DIMENSIONAL PROPERTIES OF THE STUDIED  
THREE-PHASE 28-POLE PM MOTOR PROTOTYPE

Parameter	Value	Unit
Rated power	100	kW
Rated speed	3,000	rpm
Airgap	0.5	mm
Stator outer diameter	235	mm
Stack length	127	mm
Active mass	42	kg
No. of rotor protrusions	14	–
No. of coils per phase	4	–
No. of turns per coil per phase	6	–

the values of d- and q-axes inductances [10]. The induced voltage,  $V$ , in a permanent magnet machine can be related to the back-EMF,  $\omega\lambda_{pm}$ , and machine parameters, including the winding resistance,  $R_s$ , the inductance of the direct axis,  $L_d$ , and quadrature axis,  $L_q$ , and the direct and quadrature axis currents  $I_d$ ,  $I_q$ . From the phasor diagram of PM machines, a relationship can be obtained as:

$$V_d = R_s I_d - \omega L_q I_q, \quad (10)$$

$$V_q = R_s I_q + \omega \lambda_{pm} + \omega L_d I_d, \quad (11)$$

$$V = V_d + jV_q, \quad (12)$$

and the current of the motor is given as:

$$I = I_d + jI_q. \quad (13)$$

Utilizing FEA, the values of induced voltage, back-EMF, and phase current along with their phases can be determined. With currents applied to the d- and q-axes, the aforementioned equation provides the reactance for these axes, enabling the calculation of the corresponding inductances.

A second approach for the calculation of the inductances is the use of the Park transformation ( $P_T$ ), such that the self (e.g.  $L_{aa}$ ) and mutual (e.g.  $L_{ab}$ ) inductances of the three-phase windings are obtained from the FEA. A Fourier analysis of the inductance profiles then provides expressions for self and mutual inductances given by:

$$\begin{cases} L_{aa}(\theta) = L_{sa} + L_{sv} \cos(2\theta) \\ L_{bb}(\theta) = L_{sa} + L_{sv} \cos(2\theta + 2\pi/3) \\ L_{cc}(\theta) = L_{sa} + L_{sv} \cos(2\theta - 2\pi/3) \\ L_{ab}(\theta) = -L_{ma} + L_{mv} \cos(2\theta - 2\pi/3) \\ L_{bc}(\theta) = -L_{ma} + L_{mv} \cos(2\theta) \\ L_{ca}(\theta) = -L_{ma} + L_{mv} \cos(2\theta + 2\pi/3) \end{cases}, \quad (14)$$

For a matrix of these inductances,  $L_{abc}$ , the d- and q-axes inductances can be calculated by:

$$L_{dq0} = P_T L_{abc} P_T^{-1}. \quad (15)$$

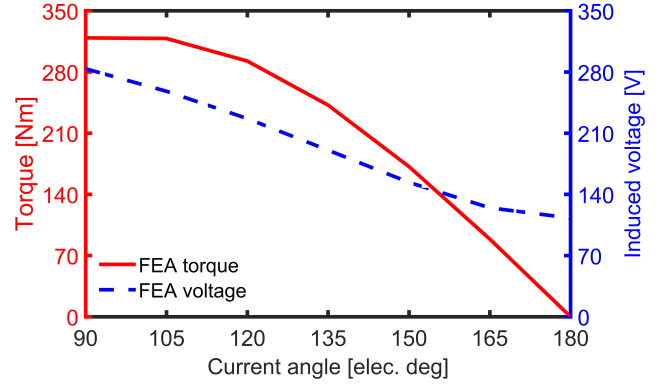


Fig. 5. The lack of saliency and hence no reluctance torque is shown through analysis of the electromagnetic torque and induced voltage using FEA.

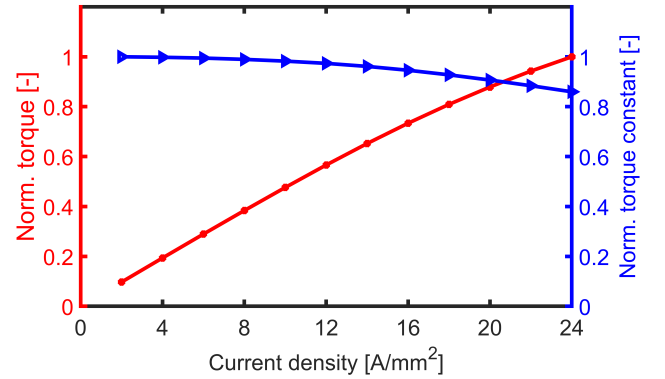


Fig. 6. Torque and torque constant vs. the current density, to show the effect of the non-linearity as a result of the armature current. Torque and torque constant are normalized based on the peak torque at the maximum current density.

The values for d- and q-axis inductances using the first method are  $123.9\mu\text{H}$  and  $125.8\mu\text{H}$ , and using the second method are  $125.1\mu\text{H}$  and  $124.6\mu\text{H}$ , respectively. The absolute percentage difference in the results of these methods for d- and q-axes inductance values is 0.9% for both cases. With nearly equal d- and q-axes inductances in this machine, according to:

$$T_e = \frac{3}{2}p [\lambda_{pm} i_q + (L_d - L_q) i_d i_q], \quad (16)$$

the reluctance component of the torque is negligible. This is confirmed by a sweep of the electromagnetic torque and voltage curves obtained from the 2-D FEA model with increasing current angle as depicted in Fig. 5. Therefore, the concept of an equivalent large airgap can be applied to this machine due its non-salient behavior despite its reluctance rotor. This hypothetical simplification can reduce the complexity of analysis and design for machines with this property allowing the use of standard analytical methods developed for uniformly-gaped machines [9], [20], [21].

There is a non-linearity in the torque constant and torque of the studied machine as a result of the interaction between the PM and armature reaction excitation fields. The non-linear

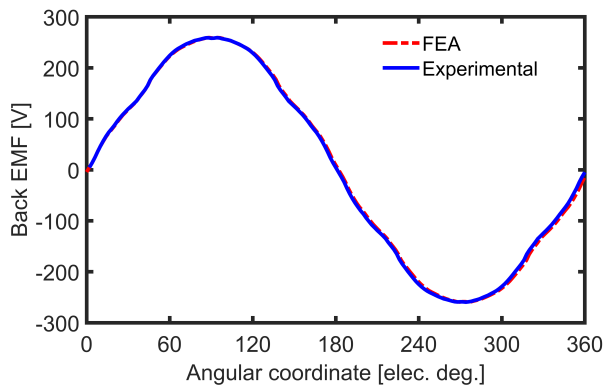


Fig. 7. Comparison of experimental and FEA results for the phase voltage of the PM prototype showing good correlation. The phase voltage values are shown for one electric period and rotor speed of 5,000rpm.

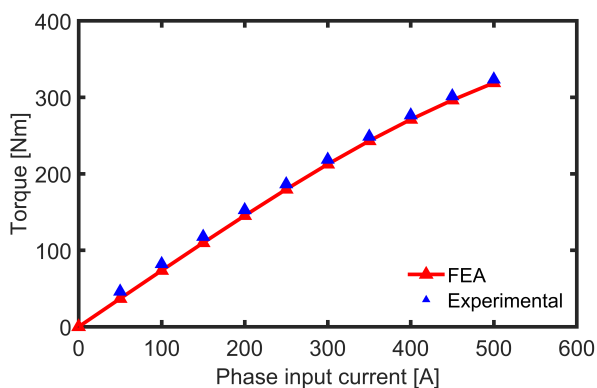


Fig. 8. A plot of the static torque with increasing phase currents. The three-phase windings are connected in a star configuration. DC current is applied to the windings such that it is equal to the peak of the AC current applied in simulations.

behavior and saturation can be observed in the normalized torque and torque constant curves as shown in Fig. 6 at very high values of current density.

The prototype for the studied machine has been fabricated as shown in Fig. 1c and its performance is further evaluated by comparing results obtained from 2D FEA analysis with those from experimental tests. The back-EMF for one phase shown in Fig. 7 was obtained by testing the prototype in open circuit condition while the results of static torque measurements at various phase input currents are shown in Fig. 8.

High-efficiency performance is possible as seen from the measured values obtained at high operating temperature in Fig. 9. Overall, a good correlation is obtained between 2D FEA and experimental results for this machine which confirms that the FEA model is an accurate representation of the prototype under investigation.

#### IV. CONCLUSION

The general theory for machines with hybrid excitation is developed using mathematical formulations and 2D FEA. The mmf of toroidal windings which cannot be explained through

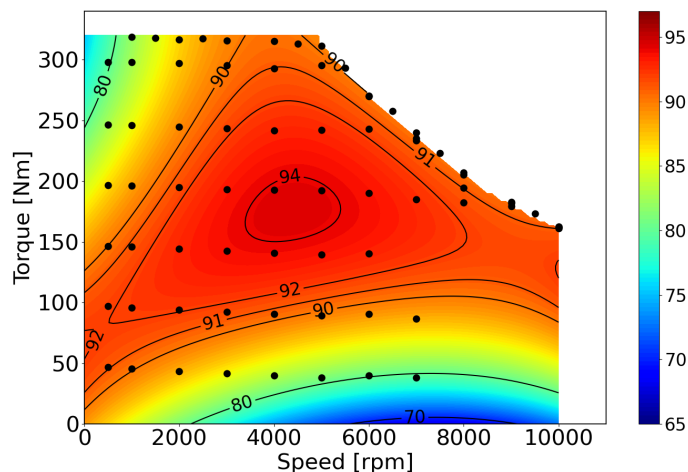


Fig. 9. Measured efficiency map of the prototype machine at high operating temperature.

the conventional mmf theory approach is developed and analyzed to reveal the feasible polarities of this synchronous machine. The harmonic decomposition of the open-circuit airgap flux confirmed that this machine's dominant principal pole pair is a final consequence of the selected number of rotor protrusions.

The studied motor topology shows non-linearity at very high values of current density due to the interaction of PM and armature fields as well as a non-salient behavior despite its castellated rotor resulting in an equivalent constant air gap. Furthermore, experimental results obtained from the motor prototype show a good correlation with those obtained from FEA thereby validating the analytical model.

#### ACKNOWLEDGMENT

This paper is based upon research sponsored by QM Power, Inc. The support of ANSYS Inc., and University of Kentucky the L. Stanley Pigman Chair in Power Endowment is also gratefully acknowledged.

#### REFERENCES

- [1] M. Rosu, P. Zhou, D. Lin, D. M. Ionel, M. Popescu, F. Blaabjerg, V. Rallabandi, and D. Staton, *Multiphysics simulation by design for electrical machines, power electronics and drives*. John Wiley & Sons, 2017.
- [2] Q. Shen, Z. Zhou, S. Li, X. Liao, T. Wang, X. He, and J. Zhang, "Design and analysis of the high-speed permanent magnet motors: A review on the state of the art," *Machines*, vol. 10, no. 7, p. 549, 2022.
- [3] B. Fahimi, L. H. Lewis, J. M. Miller, S. D. Pekarek, I. Boldea, B. Ozpineci, K. Hameyer, S. Schulz, A. Ghaderi, M. Popescu, B. Lehman, and D. D. Patel, "Automotive electric propulsion systems: A technology outlook," *IEEE Transactions on Transportation Electrification*, pp. 1–1, 2023.
- [4] M. H. Severson, R. T. Nguyen, J. Ormerod, and S. Williams, "An integrated supply chain analysis for cobalt and rare earth elements under global electrification and constrained resources," *Resources, Conservation and Recycling*, vol. 189, p. 106761, 2023.

- [5] K.-H. Kim, H.-I. Park, S.-M. Jang, D.-J. You, and J.-Y. Choi, "Comparative study of electromagnetic performance of high-speed synchronous motors with rare-earth and ferrite permanent magnets," *IEEE Transactions on Magnetics*, vol. 52, no. 7, pp. 1–4, 2016.
- [6] M. R. Hoyt, G. I. Falcon, C. J. Pearce, R. E. Delaney, T. E. Stevens, E. M. Johnson, T. M. Szenderski, N. R. Sorenson, S. F. Fultz-Waters, M. A. Rodriguez *et al.*, "Fabrication and characterization of net-shaped iron nitride-amine-epoxy soft magnetic composites," *Frontiers in Materials*, vol. 10, p. 1258382.
- [7] E. Sayed, S. M. Castano, J. W. Jiang, J. Liang, G. Pietrini, M. H. Bakr, A. Emadi, and B. Bilgin, "Design of multilayer concentric ferrite-magnet machines for a traction application," *IEEE Transactions on Transportation Electrification*, vol. 7, no. 3, pp. 1548–1560, 2021.
- [8] A. Mohammadi, O. A. Badewa, Y. Chulaee, D. D. Lewis, S. Essakiappan, M. Manjrekar, and D. M. Ionel, "Design optimization of a direct-drive wind generator with a reluctance rotor and a flux intensifying stator using different PM types," *IEEE Transactions on Industry Applications*, pp. 1–10, 2024.
- [9] D. Ionel, J. Eastham, and T. Betzer, "Finite element analysis of a novel brushless DC motor with flux barriers," *IEEE Transactions on Magnetics*, vol. 31, no. 6, pp. 3749–3751, 1995.
- [10] A. Mohammadi, Y. Chulaee, A. M. Cramer, I. G. Boldea, and D. M. Ionel, "Large-scale design optimization of an axial-flux vernier machine with dual stator and spoke PM rotor for EV in-wheel traction," *IEEE Transactions on Transportation Electrification*, vol. 10, pp. 1–12, 2024.
- [11] A. Fatemi, D. M. Ionel, M. Popescu, Y. C. Chong, and N. A. O. Demerdash, "Design optimization of a high torque density spoke-type PM motor for a formula E race drive cycle," *IEEE Transactions on Industry Applications*, vol. 54, no. 5, pp. 4343–4354, 2018.
- [12] Y. Liao, F. Liang, and T. Lipo, "A novel permanent magnet motor with doubly salient structure," *IEEE Transactions on Industry Applications*, vol. 31, no. 5, pp. 1069–1078, 1995.
- [13] H. Chen, A. M. EL-Refai, and N. A. O. Demerdash, "Flux-switching permanent magnet machines: A review of opportunities and challenges—part I: Fundamentals and topologies," *IEEE Transactions on Energy Conversion*, vol. 35, no. 2, pp. 684–698, 2020.
- [14] O. A. Badewa and D. M. Ionel, "Comparative analysis of motors with inner and outer reluctance rotors and PM stators," in *2024 IEEE Transportation Electrification Conference and Expo (ITEC)*, 2024, pp. 1–6.
- [15] Ansys® *Electronics Desktop, Maxwell, version 23.2, 2023, ANSYS Inc.*
- [16] O. A. Badewa, A. Mohammadi, D. D. Lewis, D. M. Ionel, S. Essakiappan, and M. Manjrekar, "Optimization of an electric vehicle traction motor with a PM flux intensifying stator and a reluctance outer rotor," in *2023 IEEE Transportation Electrification Conference & Expo (ITEC)*, 2023.
- [17] D. Ionel, M. Cistelecan, T. Miller, and M. McGilp, "A new analytical method for the computation of air-gap reactances in 3-phase induction motors," in *Conference Record of 1998 IEEE Industry Applications Conference. Thirty-Third IAS Annual Meeting (Cat. No.98CH36242)*, vol. 1, 1998, pp. 65–72 vol.1.
- [18] Y. G. Kang, D. Reigosa, B. Sarlioglu, and R. D. Lorenz, "D- and q-axis inductance estimation and self-sensing condition monitoring using 45° angle high-frequency injection," *IEEE Transactions on Industry Applications*, vol. 57, no. 1, pp. 506–515, 2021.
- [19] M. H. Rashid, H. A. Toliyat, M. Abolhassani, P. Niazi, and L. Hao, "Dsp-based control of variable speed drives," in *Power Electronics Handbook*. Elsevier, 2024, pp. 1261–1281.
- [20] R. Qu and T. Lipo, "Analysis and modeling of air-gap and zigzag leakage fluxes in a surface-mounted permanent-magnet machine," *IEEE Transactions on Industry Applications*, vol. 40, no. 1, pp. 121–127, 2004.
- [21] M. Cheng, P. Han, and W. Hua, "General airgap field modulation theory for electrical machines," *IEEE Transactions on Industrial Electronics*, vol. 64, no. 8, pp. 6063–6074, 2017.